Steady finite-Reynolds-number flows in three-dimensional collapsible tubes

Hazel, Andrew L. and Heil, Matthias

2003

MIMS EPrint: **2006.234**

Manchester Institute for Mathematical Sciences
School of Mathematics

The University of Manchester

Reports available from: http://eprints.maths.manchester.ac.uk/
And by contacting: The MIMS Secretary
School of Mathematics
The University of Manchester
Manchester, M13 9PL, UK

ISSN 1749-9097

J. Fluid Mech. (2003), *vol.* 486, *pp.* 79–103.
DOI: 10.1017/S0022112003004671 Printed in the United Kingdom

Steady finite-Reynolds-number flows in three-dimensional collapsible tubes

By ANDREW L. HAZEL AND MATTHIAS HEIL

Department of Mathematics, University of Manchester, Oxford Road, Manchester M13 9PL, UK

(Received 4 September 2002 and in revised form 23 December 2002)

A fully coupled finite-element method is used to investigate the steady flow of a viscous fluid through a thin-walled elastic tube mounted between two rigid tubes. The steady three-dimensional Navier–Stokes equations are solved simultaneously with the equations of geometrically nonlinear Kirchhoff–Love shell theory. If the transmural (internal minus external) pressure acting on the tube is sufficiently negative then the tube buckles non-axisymmetrically and the subsequent large deformations lead to a strong interaction between the fluid and solid mechanics. The main effect of fluid inertia on the macroscopic behaviour of the system is due to the Bernoulli effect, which induces an additional local pressure drop when the tube buckles and its cross-sectional area is reduced. Thus, the tube collapses more strongly than it would in the absence of fluid inertia. Typical tube shapes and flow fields are presented. In strongly collapsed tubes, at finite values of the Reynolds number, two 'jets' develop downstream of the region of strongest collapse and persist for considerable axial distances. For sufficiently high values of the Reynolds number, these jets impact upon the sidewalls and spread azimuthally. The consequent azimuthal transport of momentum dramatically changes the axial velocity profiles, which become approximately Θ-shaped when the flow enters the rigid downstream pipe. Further convection of momentum causes the development of a ring-shaped velocity profile before the ultimate return to a parabolic profile far downstream.

1. Introduction

In many physiological systems, viscous fluids are transported via networks of elastic tubes, e.g. the circulatory, pulmonary, renal and excretory systems. The moving fluid exerts a traction on the vessel walls, which can deform significantly in response. If the vessel is subjected to a sufficiently negative transmural pressure, P_{tm} (internal minus external pressure), it buckles non-axisymmetrically. In this regime, small changes in transmural pressure cause large changes in the cross-sectional area of the vessel. The accompanying changes in the fluid loading on the wall can lead to a strong fluid–structure interaction, potentially causing phenomena such as flow limitation and the development of large-displacement self-excited oscillations, manifested physiologically as wheezing and the Korotkoff sounds present during sphygmomanometry.

Most experimental studies of flow in collapsible tubes are performed using a Starling Resistor: a pressure chamber that encloses a finite-length elastic tube mounted between two rigid tubes. Flow in the Starling Resistor exhibits a rich dynamical behaviour and large-displacement self-excited oscillations of great complexity have been observed; see the recent review by Bertram (2002).

Previous theoretical and computational studies of collapsible-tube flow have been comprehensively reviewed by Heil & Jensen (2002). In brief, the earliest theoretical studies were based on spatially one-dimensional models, which captured behaviour such as flow limitation, wave propagation and the system's propensity to develop self-excited oscillations. However, these one-dimensional models rely on a large number of *ad hoc* assumptions and provide limited insight into the details of the complex interactions between the fluid and solid mechanics. In an attempt to develop a more rational model of collapsible-tube dynamics, Rast (1994) and Luo & Pedley (1995, 1996, 1998, 2000) considered the two-dimensional equivalent of a Starling Resistor, namely the flow through a channel in which a section of one wall is replaced by an elastic membrane. An important feature of this system is the development of a large region of separated flow downstream of the point of strongest collapse and the generation of vorticity waves during the self-excited oscillations. It is not clear, however, if these phenomena have any relevance in the three-dimensional system where the topology of the flow can be much more complex than in two dimensions (Lighthill 1963; Tobak & Peake 1982).

There are relatively few theoretical investigations of flow in three-dimensional collapsible tubes. Benmbarek (1997) and Naili, Thiriet & Ribreau (2002) have considered the steady flow of a Newtonian fluid through rigid tubes with geometries similar to those of buckled elastic tubes. Naili *et al.* (2002) considered the flow through a uniformly buckled cylinder, whereas Benmbarek's (1997) geometry was determined from experiments using a Starling Resistor. However, we believe that the only theoretical studies that include both the flow and the wall mechanics in three-dimensional collapsible tubes are those of Heil & Pedley (1996) and Heil (1997, 1998), who considered the steady motion of a viscous fluid through a buckled cylindrical shell at zero Reynolds number.

The present paper extends these previous studies by considering the effects of fluid inertia upon the system. The primary aim of the study is to investigate the details of the three-dimensional velocity fields, in order to determine to what extent, if at all, the flow features resemble those assumed in the lower-dimensional models. A secondary aim is to characterize the macroscopic behaviour of the system, i.e. the relationships between pressure drop and flow rate.

2. The model

We consider the steady flow of a viscous fluid through a thin-walled elastic tube of undeformed radius R, length L^*, wall thickness h, Poisson ratio ν and Young's modulus E. The fluid is assumed to be incompressible and Newtonian, with viscosity μ and density ρ, and the axial flow rate is Q^*. We formulate the problem in Cartesian coordinates, $\boldsymbol{x} = (x_1, x_2, x_3) = \boldsymbol{x}^*/R$, and use an asterisk to distinguish dimensional quantities from their dimensionless equivalents. The x_3-direction is chosen to lie along the tube's axis and x_1, x_2 are the transverse coordinates, see figure 1. At its upstream ($x_3^* = 0$) and downstream ($x_3^* = L^*$) ends, the elastic tube is mounted on two rigid tubes also of diameter R and of lengths $L^*_{\rm up}$ and $L^*_{\rm down}$, respectively.

2.1. *Wall equations*

We use geometrically nonlinear Kirchhoff–Love shell theory to model the deformation of the elastic tube (see e.g. Wempner 1973) . The assumptions underlying the theory are that (i) the dimensionless wall thickness h/R is small; (ii) material lines normal to the undeformed midplane remain unstretched and normal to the midplane during

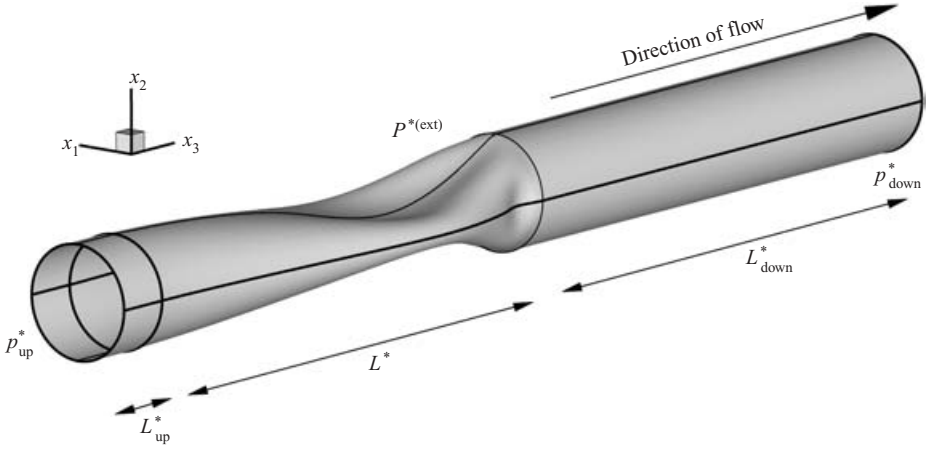

FIGURE 1. Sketch illustrating the coordinate system and the geometry of the collapsible tube. An elastic tube of lengths L^* is mounted on two rigid tubes of lengths L^*_{up} and L^*_{down}. The fluid pressure at the upstream end of the system ($x^*_3 = -L^*_{up}$) is p^*_{up}; the downstream fluid pressure (at $x^*_3 = L^* + L^*_{down}$) is p^*_{down} and the external pressure is $P^{*(ext)}$. Note the small secondary buckling pattern at the downstream end of the elastic segment.

the deformation; and (iii) the ratio of the wall thickness, h, to the minimum radius of curvature of the deformed shell remains small. Assumption (ii) implies that the deformation of the shell is completely specified by the displacements of its midplane, $\boldsymbol{v} = \boldsymbol{v}^*/R$. Lagrangian coordinates $\zeta^\alpha = \zeta^{*\alpha}/R$, where $\alpha = 1, 2$, are introduced to parameterize the midplane and its location in the undeformed configuration is given by the position vector, $\boldsymbol{r} = \boldsymbol{r}^*/R$

$$\boldsymbol{r} = (\cos(\zeta^2), \sin(\zeta^2), \zeta^1), \quad \zeta^1 \in [0, L], \quad \zeta^2 \in [0, 2\pi], \tag{1}$$

where $L = L^*/R$. The deformation of the midplane may be characterized by the strain and bending tensors, $\gamma_{\alpha\beta}$ and $\kappa_{\alpha\beta}$, respectively, defined in Appendix A, § A.1, and its position after deformation is given by

$$\boldsymbol{R}(\zeta^\alpha) = \boldsymbol{r}(\zeta^\alpha) + \boldsymbol{v}(\zeta^\alpha). \tag{2}$$

The large bending deformations of the thin-walled elastic tube that occur in the present system only generate small strains, allowing us to employ a linear constitutive equation (Hooke's law), although the theory permits the use of more general constitutive relations, see Appendix A, § A.2. The principle of virtual displacements, which describes the shell's deformation, becomes

$$\int_0^{2\pi}\int_0^L E^{\alpha\beta\gamma\delta}\left(\gamma_{\alpha\beta}\delta\gamma_{\gamma\delta} + \frac{1}{12}\left(\frac{h}{R}\right)^2 \kappa_{\alpha\beta}\delta\kappa_{\gamma\delta}\right) \mathrm{d}\zeta^1\,\mathrm{d}\zeta^2$$
$$= \frac{1}{12}\left(\frac{h}{R}\right)^3 \frac{1}{1-\nu^2}\int_0^{2\pi}\int_0^L \left(\frac{R}{h}\right) \boldsymbol{f}\cdot\delta\boldsymbol{R}\sqrt{A}\,\mathrm{d}\zeta^1\,\mathrm{d}\zeta^2, \tag{3}$$

where we use the convention that repeated indices are summed over all possible values of the index. Throughout this paper, Greek indices take the values $\alpha = 1, 2$, and Latin indices take the values $i = 1, 2, 3$. $\boldsymbol{f} = \boldsymbol{f}^*/K$ is the traction per unit area of the deformed midplane, non-dimensionalized by the bending modulus of the shell, $K = E(h/R)^3/12(1-\nu^2)$; $E^{\alpha\beta\gamma\delta}$ is the plane stress stiffness tensor, non-dimensionalized

by Young's modulus; and A is the determinant of the metric tensor of the deformed midplane, see Appendix A, § A.1.

We assume that the tube is clamped at both ends:

$$\boldsymbol{v} = \boldsymbol{0} \quad \text{at } \zeta^1 = 0, L, \tag{4a}$$

$$\partial v^r/\partial \zeta^1 = 0 \quad \text{at } \zeta^1 = 0, L, \tag{4b}$$

where v^r is the component of the displacement in the radial direction.

We now choose to resolve the displacement vector into components in the global Cartesian basis. This representation, which differs from the one used by Heil (1997), is readily extendible to more general shell geometries and also reduces the algebraic complexity of the resulting variational equations.

We decompose the domain into N_S (two-dimensional) elements and use a displacement-based finite-element method to discretize the variational equation (3), which becomes

$$\int_0^{2\pi}\int_0^{L} E^{\alpha\beta\gamma\delta}\left(\gamma_{\alpha\beta}\boldsymbol{A}_\gamma\psi^{(S)}_{,\delta} + \frac{1}{12}\left(\frac{h}{R}\right)^2\kappa_{\alpha\beta}\left[\boldsymbol{N}\psi^{(S)}_{,\gamma\delta} + \frac{\boldsymbol{A}_2\times\boldsymbol{A}_{\gamma,\delta}}{\sqrt{A}}\psi^{(S)}_{,1} - \frac{\boldsymbol{A}_1\times\boldsymbol{A}_{\gamma,\delta}}{\sqrt{A}}\psi^{(S)}_{,2}\right.\right.$$
$$\left.\left. - \frac{\boldsymbol{N}\cdot\boldsymbol{A}_{\gamma,\delta}}{A}\left\{(A_{22}\boldsymbol{A}_1 - A_{12}\boldsymbol{A}_2)\psi^{(S)}_{,1} + (A_{11}\boldsymbol{A}_2 - A_{12}\boldsymbol{A}_1)\psi^{(S)}_{,2}\right\}\right]\right)\mathrm{d}\zeta^1\,\mathrm{d}\zeta^2$$
$$= \frac{1}{12}\left(\frac{h}{R}\right)^3\frac{1}{1-\nu^2}\int_0^{2\pi}\int_0^{L}\left(\frac{R}{h}\right)\boldsymbol{f}\psi^{(S)}\sqrt{A}\,\mathrm{d}\zeta^1\,\mathrm{d}\zeta^2. \tag{5}$$

Here, $\psi^{(S)}$ are Hermite (bi-cubic) shape functions interpolating the displacements and their derivatives (Bogner, Fox & Schmit 1967). $\boldsymbol{A}_\alpha = \boldsymbol{R}_{,\alpha}$, where the comma denotes partial differentiation with respect to ζ^α. $A_{\alpha\beta} = \boldsymbol{A}_\alpha\cdot\boldsymbol{A}_\beta$ is the metric tensor of the deformed midplane and $\boldsymbol{N} = \boldsymbol{A}_1\times\boldsymbol{A}_2/|\boldsymbol{A}_1\times\boldsymbol{A}_2|$ is the (inward) unit normal to the deformed midplane.

The clamping condition (4b) was applied by imposing

$$v^1_{,1}\cos\zeta^2 + v^2_{,1}\sin\zeta^2 = 0,$$

in the form $v^1_{,1} = -v^2_{,1}\tan\zeta^2$ when $\zeta^2 \in [0, \pi/4]$ and $v^2_{,1} = -v^1_{,1}\cot\zeta^2$ when $\zeta^2 \in (\pi/4, \pi/2]$.

2.2. *Fluid equations*

We use the average axial velocity through the undeformed tube, $\bar{U} = Q^*/(\pi R^2)$, to non-dimensionalize the fluid velocity, so that $\boldsymbol{u} = \boldsymbol{u}^*/\bar{U}$, and scale the internal fluid pressure on the viscous scale, $p = p^*/(\mu\bar{U}/R)$, so that no rescaling is required to solve the equations in the absence of fluid inertia. The flow is governed by the dimensionless steady Navier–Stokes equations:

$$Re\left(u_j\frac{\partial u_i}{\partial x_j}\right) = -\frac{\partial p}{\partial x_i} + \frac{\partial}{\partial x_j}\left(\frac{\partial u_i}{\partial x_j} + \frac{\partial u_j}{\partial x_i}\right), \tag{6a}$$

and the continuity equation

$$\frac{\partial u_i}{\partial x_i} = 0, \tag{6b}$$

where $Re = \rho\bar{U}R/\mu$ is the Reynolds number.

The boundary conditions are those of no-slip on the tube walls,

$$\boldsymbol{u} = \boldsymbol{0} \quad \text{on the tube walls,} \tag{7a}$$

a prescribed fully developed Poiseuille profile upstream

$$u_1 = 0,\ u_2 = 0,\ u_3 = 2\left(1 - x_1^2 - x_2^2\right) \quad \text{at the inlet } (x_3 = -L_{\text{up}}), \tag{7b}$$

and parallel, axially traction-free outflow

$$u_1 = 0,\ u_2 = 0,\ -p + 2\frac{\partial u_3}{\partial x_3} = 0 \quad \text{at the outlet } (x_3 = L + L_{\text{down}}), \tag{7c}$$

where $L_{\text{up,down}} = L^*_{\text{up,down}}/R$. We decompose the fluid domain into N_F finite elements, within which we interpolate the velocities by tri-quadratic and the pressures by tri-linear basis functions (Taylor & Hood 1973). The discretized version of the momentum equations is based upon their weak form, generated by integrating (6*a*) over the fluid domain and using the velocity basis functions, $\psi^{(F)}$, as test functions. The viscous and pressure gradient terms are integrated by parts to give the following set of equations:

$$\iiint \left[p\frac{\partial \psi^{(F)}}{\partial x_i} - \left(\frac{\partial u_i}{\partial x_j} + \frac{\partial u_j}{\partial x_i}\right)\frac{\partial \psi^{(F)}}{\partial x_j} - Re\left(u_j\frac{\partial u_i}{\partial x_j}\right)\psi^{(F)}\right] \mathrm{d}V + \iint \left[-pn_i + \left(\frac{\partial u_i}{\partial x_j} + \frac{\partial u_j}{\partial x_i}\right)n_j\right]\psi^{(F)}\,\mathrm{d}S = 0. \tag{8a}$$

The volume integrals are evaluated over the entire fluid domain, V, and the surface integrals over the boundary of the domain, S, where $\boldsymbol{n}$ is the normal directed out of the bounding surface.

Similarly, the continuity equation (6*b*) is weighted by the pressure basis functions, $\psi^{(P)}$, to give

$$\iiint \frac{\partial u_i}{\partial x_i}\psi^{(P)}\,\mathrm{d}V = 0. \tag{8b}$$

2.3. *Fluid–solid coupling*

The fluid and solid domains interact in two ways: (i) the fluid exerts a traction on the elastic wall and (ii) the deformations of the elastic wall change the geometry of the fluid domain. An automatic mesh generation scheme, based on a variation of Kistler & Scriven's (1983) 'Method of Spines', is used to update the fluid mesh in response to changes in the wall shape. The mesh thus deforms with the tube and figure 2(*b*) shows illustrative cross-sections of the fluid mesh in a deformed tube.

The traction that the fluid exerts on the wall is part of the load terms in equations (3) and (5), which are given by

$$\boldsymbol{f} = P^{(\text{ext})}N_i - Q\left(pN_i - \left(\frac{\partial u_i}{\partial x_j} + \frac{\partial u_j}{\partial x_i}\right)N_j\right), \tag{9}$$

where $\boldsymbol{N}$ is the (inward) normal to the deformed shell midplane and $P^{(\text{ext})} = P^{*(\text{ext})}/K$ is the external pressure. The non-dimensional parameter

$$Q = \frac{\mu \bar{U}}{RK} \tag{10}$$

represents the ratio of viscous forces to the tube's bending stiffness and large values of Q indicate a strong fluid–structure interaction. The limit $Q \to 0$ corresponds to the case in which the tube's stiffness is much larger than the fluid traction, and so the tube shape is determined solely by the action of the constant external pressure, $P^{(\text{ext})}$. Q may also be interpreted as a dimensionless flow rate and, furthermore, $8Q$

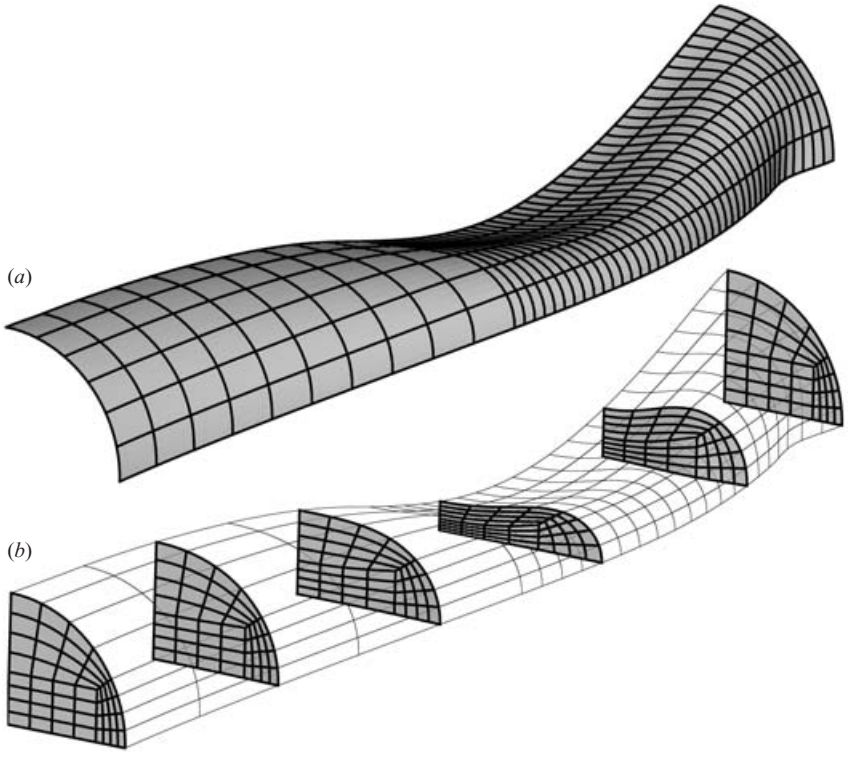

FIGURE 2. (*a*) The finite-element mesh for the shell. (*b*) Cross-sectional slices through the finite-element mesh for the fluid in the elastic section of the domain. The fluid surface mesh is indicated by light lines. The generic cross-sectional mesh deforms with changes in the wall position. It was found to be computationally efficient to choose the solid mesh such that the axial position of the nodal points coincides with the axial position of the nodal points on the surface of the fluid mesh.

is the dimensionless pressure drop, $\Delta p^*/K$, per unit length for Poiseuille flow in the undeformed tube.

If $Q = 0$, equation (9) would seem to suggest that the fluid pressure does not affect the deformation of the tube. In terms of the solid mechanics, however, an increase in the fluid pressure is completely equivalent to a decrease in the external pressure. The boundary condition (7*c*) fixes the fluid pressure at the outlet, setting it to zero. Therefore, in our model, a net change in transmural pressure is always achieved by a change in the external pressure, even when $Q \neq 0$.

2.4. *Numerical implementation*

In experiments (e.g. Conrad 1969; Bonis & Ribreau 1978), elastic tubes in Starling Resistors usually collapse into a two-lobed shape (i.e. the circumferential wavenumber is $N = 2$). Heil's (1996) stability analysis confirmed that $N = 2$ is the most unstable buckling wavenumber for tubes of sufficient length. Therefore, we restrict attention to cases in which the system is symmetric about the planes $x_1 = 0$ and $x_2 = 0$, and discretize only one quarter of the domain: $x_1 \geqslant 0$, $x_2 \geqslant 0$ and $\zeta^2 \in [0, \pi/2]$. This restriction precludes the investigation of asymmetric fluid velocity fields that may occur even in symmetric geometries (e.g. Sobey & Drazin 1986). Such an investigation would require the discretization of the entire fluid domain, at substantially higher computational cost.

The coupled nonlinear algebraic equations (5, 8*a*, *b*) were solved numerically using a Newton–Raphson method. A frontal scheme (Duff & Scott 1996) was used to assemble and decompose the Jacobian matrices. The entries of the Jacobian matrix in the fluid block were assembled analytically, but those in the solid and coupling blocks were generated by finite differencing.

It was found that the front size was minimized by placing the nodes in the shell mesh at the same axial locations as the nodes on the surface of the fluid mesh. Two Hermite shell elements (Bogner *et al.* 1967) were therefore used to cover the axial extent of one Taylor–Hood fluid element (Taylor & Hood 1973). This leads to a finer-than-necessary discretization of the shell equations. However, the increase in computational cost caused by the (modest) increase in the overall number of degrees of freedom was outweighed by a significant reduction in the number of (expensive-to-generate) entries in the interaction blocks of the Jacobian matrix.

An initial configuration in which the undeformed tube conveys Poiseuille flow was used as the initial guess for the Newton iteration. In the first computation, the transmural pressure was set to a small positive value to ensure that the system's equilibrium state was axisymmetric. The converged axisymmetric solution was then used as the initial guess for the subsequent parameter variations. In a physical experiment, the external pressure would be used as the parameter which controls the tube's collapse. However, the axisymmetric state can lose its stability to non-axisymmetric perturbations via a subcritical bifurcation (see e.g. Heil 1997 and figure 14). Therefore, we employed a displacement-control technique which specifies the degree of tube collapse by prescribing the radial displacement of a chosen control point on the shell (usually at $\zeta^1 = 0.75\,L$, $\zeta^2 = \pi/2$). This constraint is accommodated by making the external pressure, $P^{(\mathrm{ext})}$, one of the unknowns in the problem. The displacement of the control point thus becomes the control parameter in the problem and was typically varied from 0 to 85% of the tube's initial undeformed radius. In practice, the axisymmetric solution is remarkably robust and so a perturbation of the form $P_c \cos(2\zeta^2)$ was initially added to the external pressure to force the solution onto the non-axisymmetric branch. Once the tube had buckled, P_c was set to zero and the solution was recomputed before increasing the collapse further.

For typical initial guesses, the residuals are $O(1)$ and the iteration was deemed to have converged when the absolute value of the largest residual is less than 10^{-8}. A typical problem involving approximately 80 000 degrees of freedom required about fifteen minutes of CPU time per Newton iteration on a 1.4 Ghz Linux PC and convergence was generally achieved within 4 iterations.

The shell solver was validated by comparing the computed buckling loads with theoretical predictions (Yamaki 1984) and a comparison of the non-axisymmetric tube shapes under uniform pressure loading with the predictions from Flaherty, Keller & Rubinow's (1972) inextensible Euler–Bernoulli model. The results were also compared with the shell solver used by Heil (1997) to confirm that the Cartesian formulation does not affect the results.

To validate the fluid solver, we constructed velocity and pressure fields which corresponded to the flow in an axially varying tube. This flow field was made an exact solution of the Navier–Stokes equations by adding appropriate body force and source terms to (8*a*) and (8*b*), see Appendix B, § B.1. Finally, the fully coupled code was used to reproduce the previous results of Heil (1997) in the case when the Reynolds number is zero – Stokes flow. Mesh convergence of the results was confirmed by repeating selected calculations using finer discretizations, see figures 5, 14 and Appendix B, § B.2.

3. Results

In all the computations presented here, we use $L_{\text{up}} = 1$, $L = L_{\text{down}} = 10$, Poisson's ratio $\nu = 0.49$ and $h/R = 1/20$. It is convenient to introduce a new dimensionless grouping

$$H = \frac{Re}{Q} = \frac{\rho K R^2}{\mu^2}, \tag{11}$$

which depends solely upon the material parameters of the system. Thus, in any physical experiment using a given fluid and a given tube, H will be a constant. $H \to 0$ corresponds to the flow of a very viscous fluid, the case previously investigated by Heil (1997), whereas if $H > 0$ fluid inertia will affect the results. For fixed H, Q is proportional to the flow rate through the tube and it will be interpreted as such in the macroscopic parameter studies presented in § 3.3. The reported Reynolds number will be based upon the diameter of the undeformed tube $Re_D = 2\rho \bar{U} R/\mu$, as in experiments.

In all the computations, the tube was forced to buckle in such a way that the radial displacement was inwards in the plane $x_1 = 0$ and outwards in the plane $x_2 = 0$. In the subsequent sections, we shall refer to these planes as vertical ($x_1 = 0$) and horizontal ($x_2 = 0$).

In § 3.1, we demonstrate the gross effects of fluid inertia on the overall pressure distribution in the system and the deformation of the elastic tube. In the next subsection, we investigate the effects of fluid inertia on the velocity fields under two different parameter variations. In § 3.2.1, we consider a procedure in which the Reynolds number is increased by increasing the flow rate through the system, while maintaining the same degree of collapse. In contrast, § 3.2.2 describes the results when the Reynolds number is fixed, but the degree of collapse is increased by varying the external pressure relative to p_{down}, the pressure at the downstream end of the system.

The final subsection, § 3.3, is concerned with the macroscopic behaviour of the system and we analyse the dependence of the flow rate on the pressure drop through the system for two typical experimental parameter studies: (i) external pressure fixed relative to the upstream pressure (§ 3.3.1); (ii) external pressure fixed relative to the downstream pressure (§ 3.3.2).

3.1. *Effects of fluid inertia upon pressure drop and wall deformation*

Figure 3 compares the pressure distribution along the tube centreline for the flow through a strongly collapsed tube at $H = 0$ to that at $H = 1000$. In order to make a meaningful comparison, both computations were performed at the same $Q = 0.064$, the fluid pressures at the far downstream end were set to $p_{\text{down}} = 0$, and the tubes were forced to have the same degree of collapse (as specified by their vertical displacements at $\zeta^1 = 7.5$ and $\zeta^2 = \pi/2$). This last requirement was enforced by setting the external pressures to $P^{(\text{ext})} = 26.8$ for $H = 0$ and $P^{(\text{ext})} = 22.4$ for $H = 1000$. In figure 3, these values are shown as symbols and indicate the axial position downstream of which the tube becomes subject to a compressive transmural pressure.

In both cases, the upstream half of the elastic tube is only slightly deformed, hence the pressure gradient is approximately equal to that for Poiseuille flow in a rigid circular tube i.e. $\partial p/\partial x_3 \approx 8Q = 0.51$. Once $x_3 > 5$ the tube begins to buckle non-axisymmetrically, the cross-sectional area decreases and the viscous flow resistance increases dramatically. In the case when $H = 1000$, the viscous pressure drop is augmented by the Bernoulli effect via the increase in fluid velocity and the pressure is lowest at the point of strongest collapse, $x_3 \approx 7.5$. Once the tube begins to reopen,

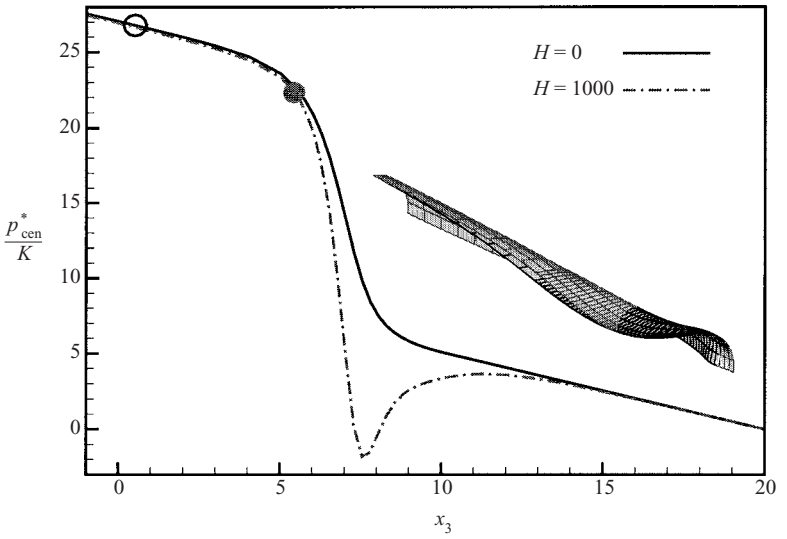

FIGURE 3. Pressure distribution along the tube centreline for two different values of H. In both cases $Q = 0.064$. The point at which the transmural pressure, P_{tm}, is zero is marked in each case (open circle $H = 0$, closed circle $H = 1000$) and the corresponding tube shapes are also shown. At $H = 1000$ the tube is more inflated at the upstream end.

the fluid velocity decreases and, in the case with fluid inertia, considerable pressure recovery is achieved. In the downstream rigid section, the pressure gradient approaches the Poiseuille value, although when $H = 1000$ this does not occur until $x_3 \approx 15$.

The difference in the internal pressure distribution for the two cases is responsible for the slight variation in the tube shapes, illustrated by the inset in figure 3. The Bernoulli effect causes the fluid pressure for $H = 1000$ to remain consistently below that for $H = 0$. If both tubes were subject to the same external pressure, the tube with $H = 1000$ would therefore be more strongly compressed. To compensate for this effect, the tube with $H = 1000$ was subjected to a smaller external pressure. In consequence, the tube is only compressed in the region $x_3 > 5.5$ and remains inflated upstream. Conversely, when $H = 0$ the tube is subject to a compressive load over most of its length ($x_3 > 0.5$).

3.2. *Velocity fields*

In this section, we present details of the velocity fields, paying particular attention to the degree of three-dimensionality in the flow, in order to assess to what extent it might affect the validity of the approximate lower-dimensional models.

3.2.1. *Effects of flow rate for a fixed degree of collapse*

Figure 4 shows contours of the axial velocity in three strongly collapsed tubes for $Re_D = 64, 191, 350$. The contours are shown in the horizontal and vertical planes of symmetry and in a number of cross-sectional planes. In all cases $H = 10^4$, so the Reynolds number is increased by increasing the flow rate. Hence, the increase in Re_D is accompanied by an increase in the viscous pressure drop along the tube, see figure 5(a). Once again, the external pressure was adjusted so that the maximum radial displacement is the same in all three cases, see figure 5(b). As a result, the increase in Re_D causes a decrease in the length of the region over which the tube is compressed and the compressive load in this region increases dramatically. When $Re_D = 350$ the

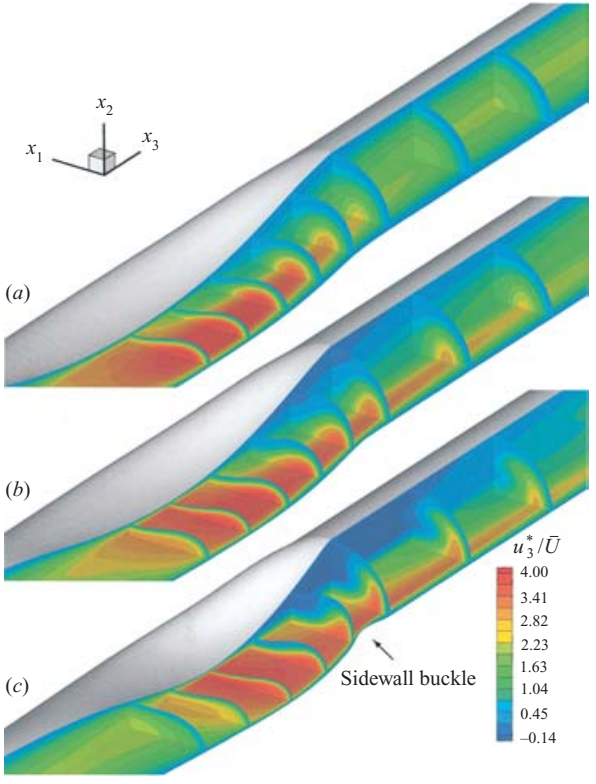

FIGURE 4. For legend, see facing page.

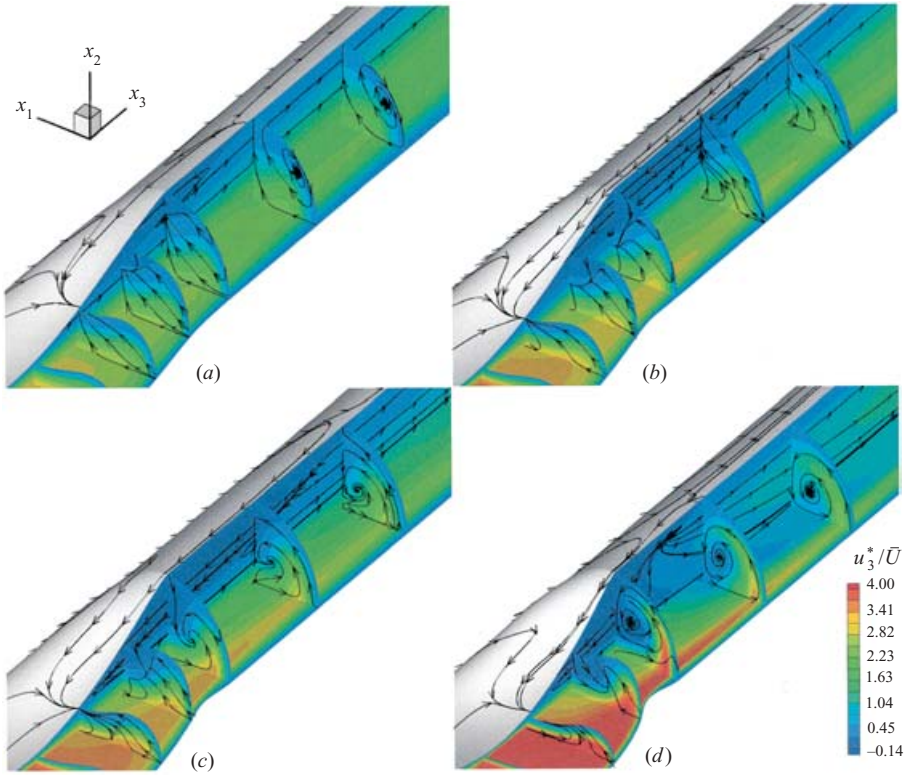

FIGURE 9. For legend, see facing page.

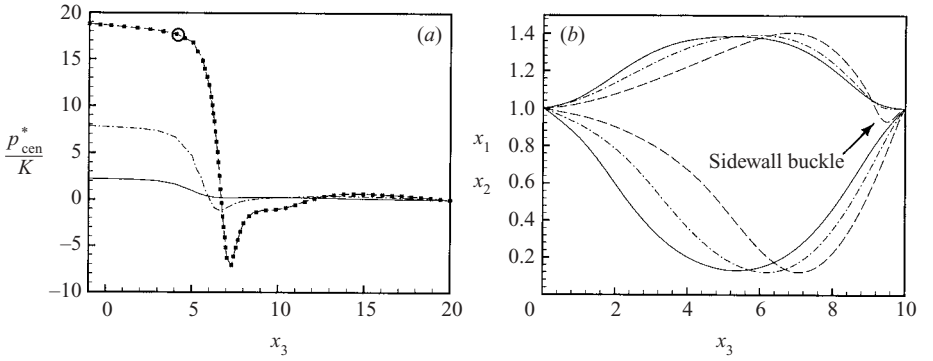

FIGURE 5. (*a*) Fluid pressure along the centreline as a function of axial distance, x_3, for $H = 10^4$ and three different Reynolds numbers, $Re_D = 64$ (solid), 191 (dash-dot), 350 (dashed). The results for a finer fluid discretization are overlaid as symbols for $Re_D = 350$. The open circle shows the point where $P_{tm} = 0$ for $Re_D = 350$ (P_{tm} is always negative for $Re_D = 64, 191$). (*b*) Wall shapes in the symmetry planes $x_1 = 0$ (lower lines) and $x_2 = 0$ (upper lines) as a function of axial distance, x_3 for $Re_D = 64$ (solid), 191 (dash-dot), 350 (dashed). A secondary buckling of the sidewall is observed when $Re_D = 350$.

compressive load near the downstream end of the tube has become so large that the sidewalls of the tube also buckle inwards. This secondary buckling pattern can also be seen in figure 1.

The flow field when $Re_D = 64$, figure 4(*a*), is similar to that already presented by Heil (1997) for Stokes flow. In the most strongly collapsed part of the tube, the point of maximum axial velocity moves from the tube's centreline into the two outer lobes which offer less flow resistance than the strongly collapsed central part of the cross-section. The fluid velocity on the tube's centreline is strongly reduced while the peak velocity increases owing to the reduction in cross-sectional area in the buckled tube. The two regions of high axial velocity that develop in the buckled region only persist for a short distance into the rigid tube and the centreline velocity returns to within 1% of the Poiseuille value by $x_3 \approx 13.2$.

At $Re_D = 191$, the flow rate has increased and the point of strongest collapse has moved further downstream, leading to a steeper wall slope in the reopening region, see also figure 5(*b*). Compared to the case when $Re_D = 64$, the reduction in the centreline velocity is less pronounced and the velocity profile in the most strongly collapsed section of the tube is much more blunt. This is a consequence of the greater axial momentum of the fluid, which opposes the viscous retardation. The Reynolds number and wall slope are so large that a region of reversed flow develops downstream of the point of strongest collapse. The areas of high axial velocity that develop in the two lobes now develop into two 'jets' and persist for much greater axial distances. In the

FIGURE 4. Contours of axial velocity, u_3, for $H = 10^4$ and (*a*) $Re_D = 64$, (*b*) 191, (*c*) 350. In all cases the minimum cross-sectional area is approximately the same and $P^{(ext)} = 9, 11.3, 17.6$, respectively.

FIGURE 9. Contours of axial velocity, u_3, for $H = 10^4$ and $Re_D = 350$ and (*a*) $P^{(ext)} = 9.02$, (*b*) $P^{(ext)} = 11.3$, (*c*) $P^{(ext)} = 13.6$ and (*d*) $P^{(ext)} = 25.8$. Also shown are streamlines in the transverse cross-sections and vertical symmetry plane and lines of skin friction on the tube wall.

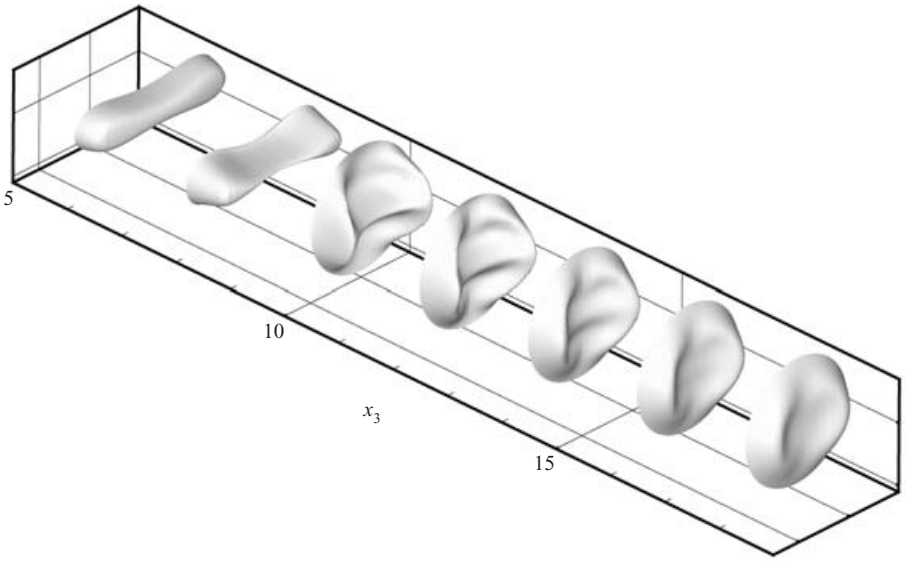

FIGURE 6. Axial velocity profiles for $H = 10^4$, $Re_D = 350$ and $P^{(\mathrm{ext})} = 17.6$ at $x_3 = 6, 8, 10, 12, 14, 16, 18$. A dimensionless velocity of $u_3 = 1$ corresponds to a distance of 0.16 along the x_3-axis.

downstream rigid tube, the axial momentum in the jets diffuses back across the tube. However, the evolution towards a Poiseuille profile occurs much more slowly than at $Re_D = 64$ and the centreline velocity is still 20% lower than the Poiseuille value by the end of the rigid tube ($x_3 = 20$).

At the highest Reynolds number shown, $Re_D = 350$, the point of strongest collapse moves even further downstream and the region of reversed flow increases in extent. The jets also persist for longer axial distances and impinge on the vertical sidewalls of the tube, which causes the jets to flatten and spread azimuthally. The fluid pressure in the region of impingement is approximately uniform across the tube, indicating that the spreading of the jets is driven by a balance between fluid inertia and viscous dissipation, rather than by a transverse pressure gradient. This type of flow structure has previously been observed experimentally by Bertram & Godbole (1997), who measured the steady flow through a rigid tube that had been deformed into the shape of a typical collapsed tube. The Reynolds number in the experiments was 705, yet the flow development appears to be essentially the same as found here: to whit, a blunt velocity profile in the region of strongest collapse, followed by the development of two pronounced jets with reversed flow between them until ultimately "a complete ring of high-magnitude velocity [...] surrounds a large central region of relatively insignificant flow" (Bertram & Godbole 1997).

The development of the ring structure can be seen in figure 6, which shows the axial velocity profiles in a number of cross-sections through the tube. On exit from the elastic tube, the velocity profile takes the shape of a Θ, with regions of high velocity in the circumferential ring and across the tube centreline in the horizontal plane $x_2 = 0$. The centreline velocity decreases as the jets spread and the velocity profile becomes more 'O'-shaped by $x_3 = 16$. Diffusion of momentum will eventually restore the velocity to a parabolic Poiseuille profile; however the centreline velocity is still 30% lower than that of Poiseuille flow at $x_3 = 20$. Our resolution of these flow features

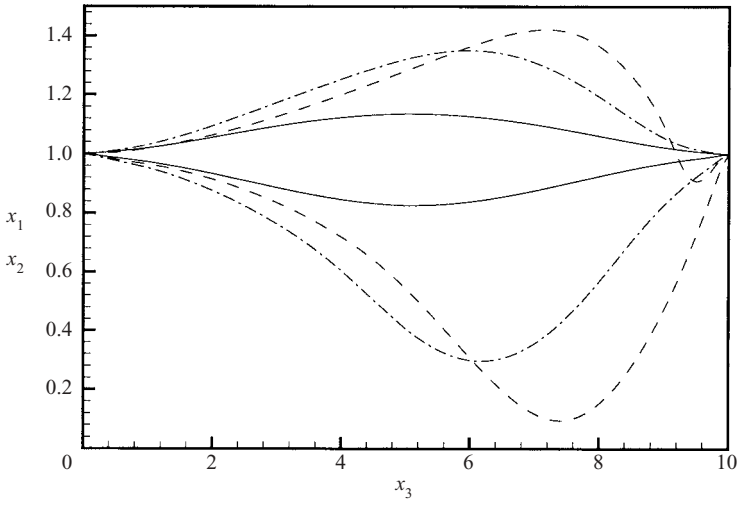

FIGURE 7. Wall shapes in the symmetry planes $x_1 = 0$ (lower lines) and $x_2 = 0$ (upper lines) as a function of axial distance, x_3. The sets of three curves are for $P^{(\mathrm{ext})} = 7.7$ (solid), 7.9 (dash-dot), 25.8 (dashed). $Re = 350$ and $H = 10^4$.

was tested by repeating the calculations with a finer resolution, see Appendix B, § B.2 for further details.

3.2.2. *Effects of degree of collapse for a fixed flow rate*

In this section, we consider an alternative procedure in which the flow rate is fixed at a Reynolds number $Re_D = 350$ and the degree of collapse is controlled by varying the external pressure. Figure 7 shows the shape of the elastic tube in the symmetry planes $x_1 = 0$ and $x_2 = 0$ at three different values of $P^{(\mathrm{ext})}$. If the degree of collapse is small, the point of strongest collapse is close to the centre of the tube, as it would be under uniform external loading. As the tube collapses further, the viscous pressure drop increases and the point of strongest collapse moves downstream.

If the axial slope of the tube wall is large enough, a strong adverse pressure gradient develops in the reopening region, leading to reversed flow near the upper and lower walls of the tube. The development of the reversed flow region is reflected by a change in the topology of the skin-friction lines, lines to which the wall-shear-stress vector is everywhere tangent (Lighthill 1963; Tobak & Peake 1982), on the tube wall, shown in figure 8. In figure 8(*a*), the tube is moderately collapsed and there is no reversed flow. Hence, the lines of skin friction are all in the same direction and there are no points at which the wall shear stress is zero. In figure 8(*b*), the tube is more strongly collapsed and two points of zero wall shear stress have developed. The skin-friction lines converge at the upstream point, which is therefore a three-dimensional point of separation. The skin-friction lines diverge at the downstream point, indicating that it is a point of re-attachment. The axial distance between the separation and re-attachment points provides a measure of the length of the region of reversed axial flow, which increases as the tube collapses yet further, figure 8(*c*).

Figure 9 shows details of the flow fields near the downstream end of the elastic tube, as it collapses. Again, contours of axial velocity are shown in the horizontal and vertical symmetry planes and in a number of axial cross-sections. In addition, the skin friction lines are also shown. As the degree of collapse increases, the height

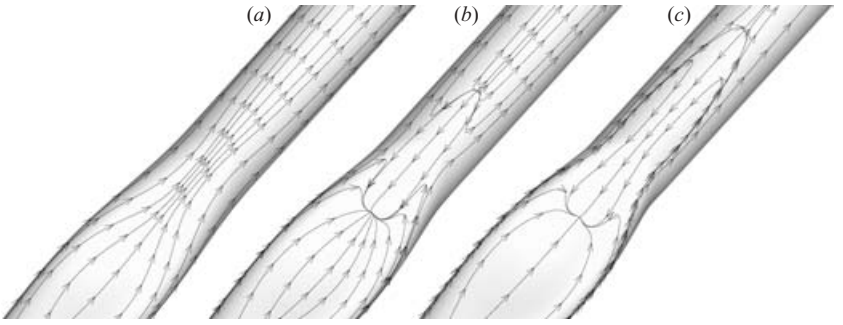

FIGURE 8. Lines of skin friction, for $H = 10^4$, $Re_D = 350$ and (*a*) $P^{(\mathrm{ext})} = 7.33$, (*b*) $P^{(\mathrm{ext})} = 9.02$ and (*c*) $P^{(\mathrm{ext})} = 11.3$. A topological change occurs after flow separation when two points of zero wall shear stress develop.

and length of the reversed flow region increase. In moderately collapsed tubes, the flow field in the tube's vertical plane of symmetry is not dissimilar to that found in two-dimensional collapsible channel flows: fluid recirculates inside a 'separation bubble' above a streamline connecting the points of separation and re-attachment. The flow in a two-dimensional plane taken from a three-dimensional flow field need not be divergence free, however, and this allows the formation of foci, see figure 9(*a*). The flow under the separation bubble has an upward ($u_2 > 0$) component in the plane $x_1 = 0$. This motion drives secondary flows in the transverse cross-sections $x_3 =$ constant and leads to the formation of weak axial vortices (maximum magnitude of transverse flows $\approx 0.05\bar{U}$).

As the tube collapses more strongly, the extent of the separation bubble increases and, accordingly, a greater proportion of the flow in the plane $x_1 = 0$ has a downward ($u_2 < 0$) component. This is reflected in the transverse flows which are directed downwards near the plane $x_1 = 0$ and change the sense of rotation of the secondary vortices, see figure 9(*c*).

As the tube collapses yet further, the height of the separation bubble increases to fill the entire tube, something that is not possible in two-dimensional channel flow. The secondary motions driven by the separation combine with the azimuthal spreading of the axial jets to generate strong axial vortices (maximum magnitude of transverse flow $\approx 0.25\bar{U}$ in figure 9*d*). The axial vortices transport momentum towards the top of the tube, causing the length of the reversed flow region to decrease significantly. In figure 9(*c*), the distance between the separation and re-attachment points is ~ 6.3 whereas in figure 9(*d*) it has decreased to ~ 3.8.

The nodal point (a free stagnation point) in the vertical plane in figure 9(*d*) is close to the upper wall of the tube and may be interpreted as the point at which the two azimuthally spreading jets collide, see also figure 6. The azimuthal transport of momentum following the impact of a 'jet' on a tube wall has previously been observed by Ethier *et al.* (1999) who studied flow in a 45° junction (e.g. see their figure 10). In that geometry the collision of the jets (termed secondary-flow boundary layers by Ethier *et al.*) on the upper wall was postulated as the mechanism for flow separation upstream of the point of collision. Figure 9(*a*) indicates that, in the collapsible tube, flow separation can occur without collision of the jets. Furthermore, in contrast to Ethier *et al.*'s (1999) findings, the collision of the jets after a relatively short axial distance in figure 9(*d*) could be said to inhibit flow separation as it causes a reduction in length of the region of reversed flow.

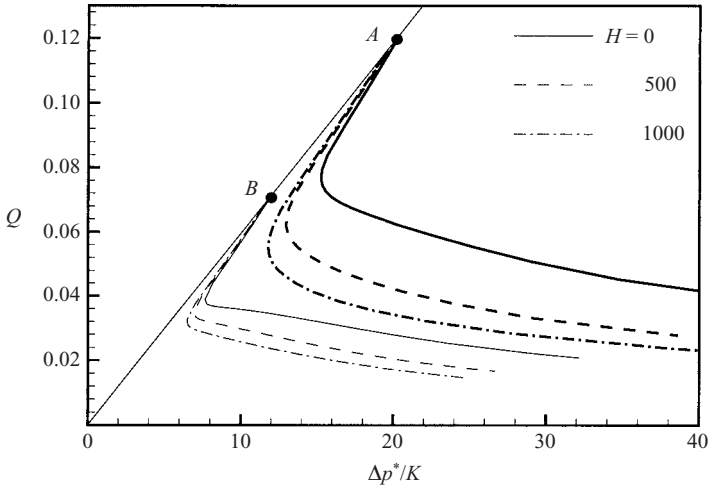

FIGURE 10. Volume flux, Q, as a function of pressure drop, $\Delta p = p_{\mathrm{up}} - p_{\mathrm{down}}$, for constant upstream transmural pressure. The different line thickness denotes two different upstream transmural pressures: $P_{\mathrm{tm(up)}} = 0$ (thick) and -2.5 (thin). The points at which the axisymmetric state becomes unstable to non-axisymmetric perturbations is indicated by A ($P_{\mathrm{tm(up)}} = 0$) and B ($P_{\mathrm{tm(up)}} = -2.5$).

3.3. *Macroscopic parameter studies*

In this subsection we consider the effects of fluid inertia upon the macroscopic behaviour of the system. In particular, we consider the relationship between the pressure drop and flow rate through the tube. We investigate the cases in which either the upstream or downstream transmural pressure is held constant. The upstream and downstream transmural pressures are taken to be those at the ends of the system, i.e. at the ends of the rigid tubes, see figure 1. In experiments, these pressures, in particular the downstream pressure, are often measured nearer the ends of the elastic tube, which, although changing the quantitative results, does not affect the qualitative behaviour of the system.

3.3.1. *Fixed upstream transmural pressure*

First, we consider the case when the upstream transmural pressure ($P_{\mathrm{tm(up)}} = p_{\mathrm{up}} - P^{(\mathrm{ext})}$) is held constant. This corresponds to an experimental procedure in which the upstream end of the tube is connected to a large constant-head reservoir, while the flow is driven by lowering the pressure p_{down} at the downstream end.

If there is no flow, there is no pressure drop and the entire tube is subjected to a constant transmural pressure. The tube's buckling pressure, under zero flow conditions, is approximately -6, and hence, at $\Delta p = 0$, the tube's deformation is axisymmetric for both the cases shown in figure 10 ($P_{\mathrm{tm(up)}} = 0, -2.5$). For small increases in the pressure drop, the wall remains axisymmetric and, because the axisymmetric deformations are small, the flow rate increases approximately linearly in accordance with Poiseuille's law. An increase in the pressure drop causes the transmural pressure at the downstream end of the elastic tube to become increasingly negative and when it falls below a critical value (indicated by the points A and B in figure 10), the tube buckles and the system bifurcates subcritically. If Δp is held constant during the buckling, the tube jumps (dynamically) into a strongly collapsed equilibrium configuration. The buckled tube has a much greater flow resistance and

hence the flow rate through the system decreases during the bifurcation. Any further increase in Δp causes a reduction in the flow rate – a phenomenon known as 'negative effort dependence'. If the external pressure is increased, corresponding to a lower value of $P_{\mathrm{tm(up)}}$, a smaller viscous pressure drop is required to reach the critical buckling pressure and hence the bifurcation point moves closer to the origin, as previously demonstrated for Stokes flow by Heil (1996, 1997) and observed experimentally by Bertram & Castles (1999).

As seen in § 3.1, the inclusion of fluid inertia causes an additional local pressure drop due to the Bernoulli effect. Thus, when the axisymmetric solution loses stability, the tube becomes more strongly collapsed, with an additional decrease in the flow rate. The position of the bifurcation point at any given value of $P_{\mathrm{tm(up)}}$ remains approximately unchanged, however, because it is determined by the loading on the elastic tube, which is hardly affected by fluid inertia while the tube remains axisymmetric. An increase in H increases the 'strength' of the Bernoulli effect and causes an increased collapse at a given pressure drop. The Bernoulli effect is more pronounced at higher flow rates (higher Reynolds numbers) and hence the inertial effects are less pronounced at more negative upstream transmural pressures, where the tube buckles at lower flow rates.

Flow limitation and negative effort dependence can occur by essentially the same mechanism in any system in which an increase in Δp causes an increase in downstream collapse and the effects of the accompanying increase in flow resistance exceed those of the increase in Δp. Indeed, qualitatively similar behaviour, has been found in previous lower-dimensional models (Shapiro 1977; Luo & Pedley 2000) and has also been observed experimentally (Bonis & Ribreau 1978; Bertram & Castles 1999) over a wide range of Reynolds numbers. In the lower-dimensional models, however, the absence of a persistent, albeit unstable, axisymmetric state leads to a change in the mathematical structure of the solutions. In particular, the pressure-drop–flow-rate curves presented by Luo & Pedley (2000) for their two-dimensional model exhibit limit points, rather than subcritical bifurcations.

3.3.2. *Fixed downstream transmural pressure*

We next turn to the case in which the downstream transmural pressure is held constant. This corresponds to an experimental procedure in which the downstream end of the tube is connected to the reservoir and the flow is driven by raising the pressure upstream. We consider cases in which the external pressure is large enough to hold the tube in a buckled configuration when there is no flow. Increasing the pressure drop will now increase the transmural pressure in the elastic tube, causing it to reopen until it eventually becomes axisymmetric. At low values of the pressure drop, the flow rates are all very low and figure 11 shows that fluid inertia has little effect. Indeed for the lowest external pressure when the tube is only slightly buckled initially, the flow rates required to reopen the tube are so small that inertial effects remain completely negligible.

At greater external pressures, inertial effects begin to manifest themselves, once the flow rate is large enough. In general, a greater pressure drop is required to maintain the same flow rate as H increases. This is again due to the additional Bernoulli suction which holds the tube in a more strongly collapsed configuration at any given pressure drop. It therefore follows that a greater pressure drop is required to reopen the tube at a given external pressure compared to the Stokes flow case. Note that at the highest external pressure, the lines do not reach the origin. This is because, in these cases, the external pressure exceeds the pressure at which, in the absence of

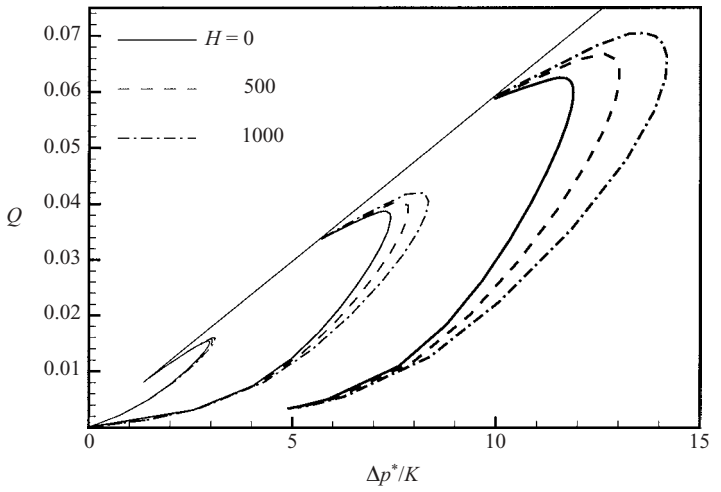

FIGURE 11. Volume flux, Q, as a function of pressure drop, $\Delta p = p_{\mathrm{up}} - p_{\mathrm{down}}$, for constant downstream transmural pressure. The different line thicknesses denote three different downstream transmural pressures: $P_{\mathrm{tm(down)}} = -7$ (thin), -10 (medium) and -13 (thick).

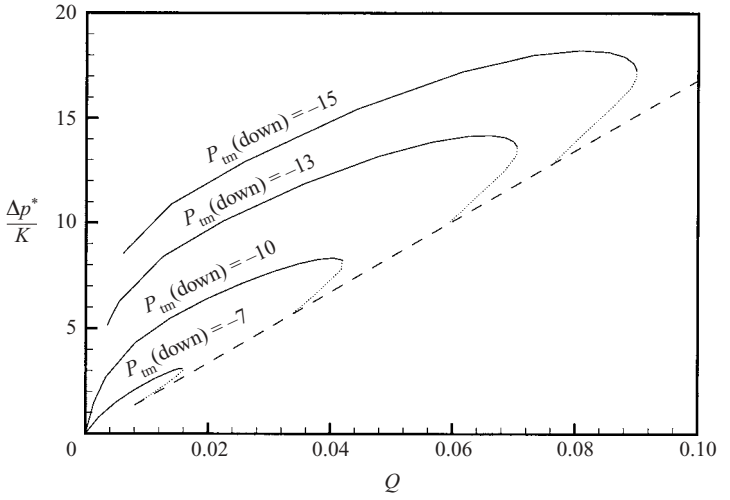

FIGURE 12. Pressure drop, $\Delta p = p_{\mathrm{up}} - p_{\mathrm{down}}$, as a function of volume flux, Q, for constant downstream transmural pressure and $H = 1000$. The axisymmetric branch is shown as the dashed line and the dotted lines represent solution branches that are unstable if the flow rate, Q, is prescribed.

flow, the elastic tube makes opposite wall contact and this effect is not included in the present numerical code.

A feature previously observed in experiments in which the downstream transmural pressure is held constant is so-called 'pressure-drop limitation', where the pressure drop becomes approximately independent of the flow rate (Brower & Scholten 1975; Bonis & Ribreau 1978; Bertram 1986). The experimental data illustrating 'pressure-drop limitation' are usually presented with Q on the abscissa and, to aid the discussion, we replot the data for $H = 1000$ in this form in figure 12.

Increasing the external pressure, equivalent to decreasing $P_{\mathrm{tm(down)}}$, causes the curves to steepen near the origin, as observed experimentally and in the one-dimensional model of Jensen & Pedley (1989). The steepening is due to the greater degree of tube collapse at higher external pressures and hence a higher initial flow resistance. After the initial rise in pressure drop, there is a region where the curves become almost parallel and their gradient is approximately equal to that of the axisymmetric solution. It is this region that has been described as exhibiting 'pressure-drop limitation'.

Typically, the experimental studies have included cases in which the external pressure is so great that the tube is strongly collapsed over its entire length, leading to higher maximum values of $\Delta p^*/K$ than in figure 12. The vertical scale in the experimental plots, e.g. figure 11 of Bonis & Ribreau (1978), is therefore greater than in figure 12, causing the gradient of the axisymmetric branch to appear closer to zero; it was this apparent shallow gradient of the pressure-drop–flow-rate curves that gave rise to the term 'pressure-drop limitation'. In these experiments, however, the tube remained buckled even at the highest flow rates, so the axisymmetric branch was never attained. Conrad (1969) considered a slightly different parameter variation (fixed downstream resistance, as opposed to fixed $P_{\mathrm{tm(down)}}$), but continued to increase the flow rate until the tube had completely reopened. In that case, the results, e.g. figure 4(*a*) in his paper, are qualitatively similar to those shown in figure 11.

The values of H in the experiments were considerably higher than those presented here, e.g. in Bonis & Ribreau's (1978) experiments, $H \approx 1.6 \times 10^6$. The consequent large Reynolds numbers, even at modest flow rates, prevents a direct comparison between the experimental data and our results. A further complication is the appearance of self-excited oscillations in this regime (Bertram 1986).

4. Discussion

In this paper, we have investigated the steady finite-Reynolds-number flow of a viscous fluid through a thin-walled elastic tube (a model Starling Resistor).

The macroscopic behaviour of the system may be completely understood by regarding the fluid pressure drop as having a viscous contribution and a further contribution due to the Bernoulli effect. This latter contribution becomes more pronounced as the flow rate (or Reynolds number) increases. In the case when the upstream transmural pressure is held constant, so that an increase in flow rate is destabilizing, the degree of collapse immediately after the axisymmetric solution loses stability increases with Reynolds number. In the case when the downstream transmural pressure is constant, so that an increase in flow rate is stabilizing, the pressure drop required to reopen the tube increases with increasing Reynolds number.

The details of the velocity field are not so simply understood and quite complex velocity profiles can develop as the Reynolds number increases. At all Reynolds numbers, once the tube is sufficiently collapsed the highest axial velocities are no longer confined the tube's centreline. The two-lobed shape of the collapsed tube drives the formation of two axial 'jets'. As the Reynolds number increases, the centreline velocity decreases more slowly and hence the development of the jets occurs over longer axial distances, but, once established, they also persist for greater distances downstream. A dramatic change in the flow field occurs when the jets impinge upon the sidewalls of the tube, after which they flatten and spread azimuthally.

In one-dimensional models, a key parameter is the speed index, S, defined to be the ratio of the average flow speed, $\bar{u}$, to the propagation speed of small-amplitude waves that travel along the tube, c (Shapiro 1977). In the one-dimensional theory, $\bar{u} = \bar{U}/\alpha$

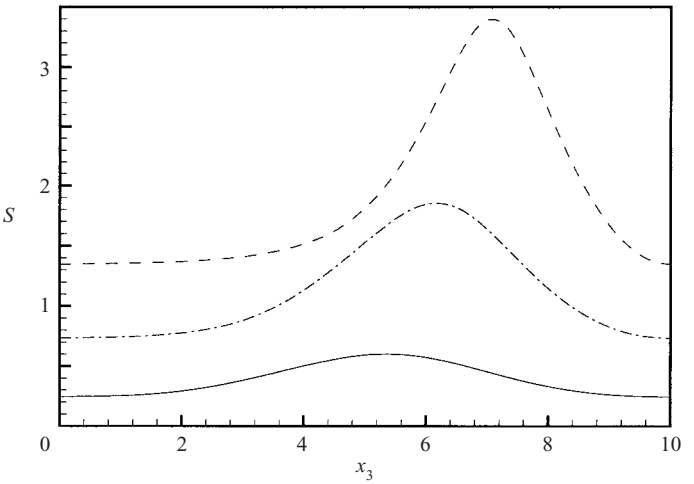

FIGURE 13. Approximate values of the speed index, S, as a function of axial distance along the elastic tube, x_3 for the results presented in § 3.2.1: $H = 10^4$ and $Re_D = 64$ (solid), 191 (dash-dot) and 350 (dashed).

and c is given by $c^2 = (\alpha K/\rho)\,\partial\mathscr{P}/\partial\alpha$, where α is the ratio of the cross-section area of the tube to the undeformed area (πR^2). $\mathscr{P}(\alpha)$ is the 'tube law', a single-valued relationship between the cross-sectional area of the tube and the local transmural pressure, which is usually approximated by the pressure–area relation of an infinitely long tube. It follows that

$$S^2 = \frac{\rho \bar{U}^2}{K}\left[\frac{1}{\alpha^3}\left(\frac{\partial\mathscr{P}}{\partial\alpha}\right)^{-1}\right] = Re\,Q\left[\frac{1}{\alpha^3}\left(\frac{\partial\mathscr{P}}{\partial\alpha}\right)^{-1}\right], \tag{12}$$

demonstrating that the local speed index is proportional to the square-root of the global parameter $Re\,Q$, which represents the ratio of fluid inertia to bending stiffness of the tube.

If $\bar{u}$ approaches c anywhere along the tube, the one-dimensional model predicts that there can be no steady solution, a phenomenon known as 'choking' which occurs when $S \to 1$. It has been speculated, therefore, that the onset of self-excited oscillations coincides with the occurrence of supercritical flow, $\bar{u} > c$, at some point along the tube.

In the present system it is possible to calculate approximate values of S as a function of the axial distance along the tube. For this purpose, the tube law for an infinite tube subject to uniform pressure loading was calculated numerically using the shell solver and $\partial\mathscr{P}/\partial\alpha$ was then determined by finite differences. The cross-sectional area of the finite-length tube was assumed to be the same as the cross-sectional area of an infinitely long tube with the same (inward) displacement in the plane $x_1 = 0$. Equation (12) was then used to calculate $S(x_3)$ for the data presented in § 3.2.1. The results are shown in figure 13, and correspond to the wall displacements and pressure drops shown in figure 5.

At the lowest Reynolds number, $S < 1$ and the flow is entirely subcritical. At $Re_D = 191$, the flow is supercritical only in the region of the constriction and at $Re_D = 350$, $S > 1$ and the flow is supercritical everywhere. Thus, steady three-dimensional

solutions can exist even when the flow becomes supercritical, although the computed steady solutions may be unstable.

Previous studies have stressed the role of flow separation. Indeed, Cancelli & Pedley (1985) proposed that the dissipation necessary to allow the development of self-excited oscillations in collapsible tube flow occurred mainly in the regions of flow separation downstream of the point of strongest collapse. The two-dimensional calculations of Luo & Pedley (1996) showed that, in fact, most of the energy is dissipated in the boundary layers upstream of the point of strongest collapse. In our three-dimensional study, we also find that the fluid dissipation is greatest near the upper and lower walls in the region of strongest collapse. At larger Re, there is also significant dissipation near the point where the high-velocity jets impinge on the sidewall, particularly if the sidewall has buckled inwards.

We further find that three-dimensional flow 'separation', as defined by a topological change in the skin friction lines, does have a significant effect on the velocity field downstream of the point of strongest collapse. For sufficiently large wall slopes, a region of reversed flow develops, increasing with Re and the degree of collapse. In this situation, the velocity field on the vertical symmetry plane is not dissimilar to that predicted by the two-dimensional studies. An important difference is that the reversed-flow region is open and can extend to fill the entire vertical symmetry plane. This is impossible in two dimensions, where the reversed-flow region is closed and cannot occupy the entire tube without violating conservation of mass. Once the reversed flow occupies the entire height of the tube, the motion of fluid towards the tube's centreline drives a transverse flow, which combines with the azimuthal spreading of the jets to create strong transverse vortices. The transverse vortices transport momentum from the two axial jets towards the upper and lower walls of the tube. This leads to a Θ-shaped velocity profile, with high velocities across the tube's horizonal plane of symmetry and in a surrounding ring. Continued convection of momentum by the vortices to the ring leads to the development of an O-shaped profile before the ultimate return to Poiseuille flow. In this regime, the flow is highly three-dimensional and any lower-dimensional model is unlikely to provide an adequate representation of the system's behaviour.

There have been few experimental measurements of velocities in three-dimensional collapsible tubes (e.g. Ohba, Sakurai & Oka 1997; Kounanis & Mathioulakis 1999) and the Reynolds numbers in these experiments are considerably higher than in our computations. It remains to be seen how the flow structures are affected by further increasing Re. Nonetheless, the development seen here appears to be very similar to that reported in Bertram & Godbole's (1997) study of steady flow in a rigid 'buckled' tube at $Re_D = 705$, although they postulated a pressure-based mechanism for the initiation of the secondary flow that leads to the formation of the high-velocity ring. In a more recent set of experiments in the same rigid model of a collapsed tube, Bertram *et al.* (2001) found that the flow at $Re_D = 5900$ was qualitatively similar to the measurements at $Re_D = 705$. Despite the fact that the flow is turbulent at $Re_D = 5900$, Bertram *et al.* (2001) observed a blunt velocity profile in the region of strongest collapse and the development of the downstream jets into "an almost complete annulus of high-speed forward flow". In contrast to our results, Bertram *et al.* (2001) observed the development of a region of reversed axial flow on tube's centreline, downstream of the region of strongest collapse. This should be interpreted as a further topological change following the situation in figure 9(*d*) and is probably a result of the combination of a high Reynolds number and a high degree of tube collapse (maximum inward displacement was $\sim$95% of the undeformed radius).

A direct comparison with experimental measurements of steady high-Re velocity fields in elastic tubes would be difficult. At large Re, symmetric steady flows are likely to be unstable and, therefore, impossible to realize experimentally. Symmetry-breaking bifurcations for flows in rigid symmetric geometries have been found in channel and pipe flows and recently Kounanis & Mathioulakis (1999) have observed symmetry breaking in three-dimensional collapsible-tube experiments. Furthermore, irrespective of its symmetry, the steady state will probably be unstable to temporal disturbances, giving rise to self-excited oscillations.

In the light of these observations, rather than extending our steady calculations to higher Reynolds numbers, a more natural continuation of the present work would be the extension to time-dependent problems, an extension that is currently in progress.

Financial support from the EPSRC is gratefully acknowledged. The HSL library routines MA42: a frontal solver for sparse, unsymmetric systems, MP42: a parallel frontal solver and the cfortran.h header file were used in the development of the numerical code in this work. The authors would also like to thank the anonymous referees for their comments and C. D. Bertram for several helpful discussions and for re-examining the data from Bertram & Godbole (1997).

Appendix A. Details of solid mechanics

A.1. *Geometrical quantities used in shell theory*

In order to characterize the geometry of the shell's undeformed midplane, we determine the base vectors $\boldsymbol{a}_\alpha = \boldsymbol{r}_{,\alpha}$, where the comma denotes partial differentiation with respect to ζ^α, and construct the covariant midplane metric tensor $a_{\alpha\beta} = \boldsymbol{a}_\alpha \cdot \boldsymbol{a}_\beta$, with determinant $a = a_{11}a_{22} - a_{12}a_{21} = 1$. We define a curvature tensor, $b_{\alpha\beta} = \boldsymbol{n} \cdot \boldsymbol{a}_{\alpha,\beta}$, where $\boldsymbol{n} = \boldsymbol{a}_1 \times \boldsymbol{a}_2 / |\boldsymbol{a}_1 \times \boldsymbol{a}_2|$ is the unit normal to the midplane.

Uppercase letters are used to denote shell variables associated with the deformed midplane and we define the deformed midplane base vectors, $\boldsymbol{A}_\alpha = \boldsymbol{R}_{,\alpha}$; deformed covariant midplane metric tensor, $A_{\alpha\beta} = \boldsymbol{A}_\alpha \cdot \boldsymbol{A}_\beta$, with determinant A; and deformed curvature tensor, $B_{\alpha\beta} = \boldsymbol{N} \cdot \boldsymbol{A}_{\alpha,\beta}$, where $\boldsymbol{N} = \boldsymbol{A}_1 \times \boldsymbol{A}_2 / |\boldsymbol{A}_1 \times \boldsymbol{A}_2|$ is the unit normal to the deformed midplane.

The strain and bending tensors are then defined to be

$$\gamma_{\alpha\beta} = \tfrac{1}{2}(A_{\alpha\beta} - a_{\alpha\beta}), \quad \kappa_{\alpha\beta} = -(B_{\alpha\beta} - b_{\alpha\beta}),$$

and the plane stress stiffness tensor is given by

$$E^{\alpha\beta\gamma\delta} = \frac{1}{2(1+\nu)} \left(a^{\alpha\gamma} a^{\beta\delta} + a^{\alpha\delta} a^{\beta\gamma} + \frac{2\nu}{1-\nu}\, a^{\alpha\beta} a^{\gamma\delta} \right), \tag{A 1}$$

where $a^{\alpha\beta}$ is the contravariant metric tensor of the undeformed midplane.

A.2. *Extension to nonlinear constitutive laws*

The principle of virtual displacements for large deformations of a three-dimensional elastic body loaded by surface tractions, $\boldsymbol{t}$ (force per unit area of the deformed surface) may be written as

$$\iiint \sigma^{ij} \delta\epsilon_{ij} \, \mathrm{d}v = \iint \boldsymbol{t} \cdot \delta\boldsymbol{v} \, \mathrm{d}A, \tag{A 2}$$

where σ^{ij} is the second Piola–Kirchhoff stress tensor, ϵ_{ij} is the Green–Lagrange strain tensor, and $\boldsymbol{v}$ is the (virtual) displacement field of the body, see e.g. Wempner (1973),

Bathe (1996). The principle applies for any general constitutive relation between the stress and strain tensors.

Equation (3) follows from using the linear constitutive equation $\sigma^{ij} = \hat{E}^{ijkl}\epsilon_{kl}$, assuming a stress-free initial state, plane stress in the midplane, and integrating through the thickness of the shell analytically, under the assumption that normals to the undeformed midplane remain unstretched and normal to the midplane during the deformation. These assumptions may also be applied to derive a shell theory for a general constitutive relation, although integration through the thickness may then have to be performed numerically.

Appendix B. Validation of numerical results

B.1. *Construction of an 'exact' solution*

In order to validate the fluid solver, we considered a rigid tube of axially varying elliptical cross-section that approximated the shape of a collapsed elastic tube. The x_3-axis was taken to be the tube's centreline and the tube had length $L = 10$ ($-5 \leqslant x_3 \leqslant 5$). The semi-axes of the ellipses were aligned with the coordinate directions x_1 and x_2 and

$$R_1 = 1 + \frac{1}{625}(x_3 - 5)^2(x_3 + 5)^2, \quad R_2 = 1 - \frac{1}{1250}(x_3 - 5)^2(x_3 + 5)^2. \tag{B 1}$$

We postulated the following velocity and pressure fields:

$$u_1^\dagger(\boldsymbol{x}) = \frac{1}{625}x_1(x_3 - 5)^2(x_3 + 5)^2\left\{1 - \left(\frac{x_1}{R_1}\right)^2 - \left(\frac{x_2}{R_2}\right)^2\right\}, \tag{B 2a}$$

$$u_2^\dagger(\boldsymbol{x}) = \frac{1}{625}x_2(x_3 - 5)^2(x_3 + 5)^2\left\{1 - \left(\frac{x_1}{R_1}\right)^2 - \left(\frac{x_2}{R_2}\right)^2\right\}, \tag{B 2b}$$

$$u_3^\dagger(\mathrm{x}) = 1 - \left(\frac{x_1}{R_1}\right)^2 - \left(\frac{x_2}{R_2}\right)^2, \tag{B 2c}$$

$$p^\dagger(\boldsymbol{x}) = 5 - x_3, \tag{B 2d}$$

which satisfy the no-slip condition at the tube walls (7*a*) and ensure parallel axially traction-free outflow (7*c*) at $L = 5$.

Equations (B 2*a–d*) were substituted into the governing equations (6*a*, *b*) to give

$$Re\left(u_j^\dagger\frac{\partial u_i^\dagger}{\partial x_j}\right) + \frac{\partial p^\dagger}{\partial x_i} - \frac{\partial}{\partial x_j}\left(\frac{\partial u_i^\dagger}{\partial x_j} + \frac{\partial u_j^\dagger}{\partial x_i}\right) = F_i^\dagger, \tag{B 3a}$$

$$\frac{\partial u_i^\dagger}{\partial x_i} = Q^\dagger. \tag{B 3b}$$

The resulting body-force terms, $F_i^\dagger$, and the mass-source term, $Q^\dagger$, were added to the weak form of the governing equations (8*a*, *b*), leading to one additional term in each equation

$$\iiint F_i^\dagger\psi^{(F)}\,\mathrm{d}V, \quad \iiint Q^\dagger\psi^{(P)}\,\mathrm{d}V, \quad \text{respectively.}$$

The augmented system of equations was solved numerically by the method described in § 2.4, but without any fluid–structure interaction. The values of the postulated velocity field at $x_3 = -5$ were used as a Dirichlet boundary conditions at the inlet.

Approx. no. of degrees of freedom	$\mathscr{E}$
10 000	0.033
40 000	0.00068
60 000	0.00043

TABLE 1. Values of the global error norm, $\mathscr{E}$, at three different mesh resolutions for $Re = 350$.

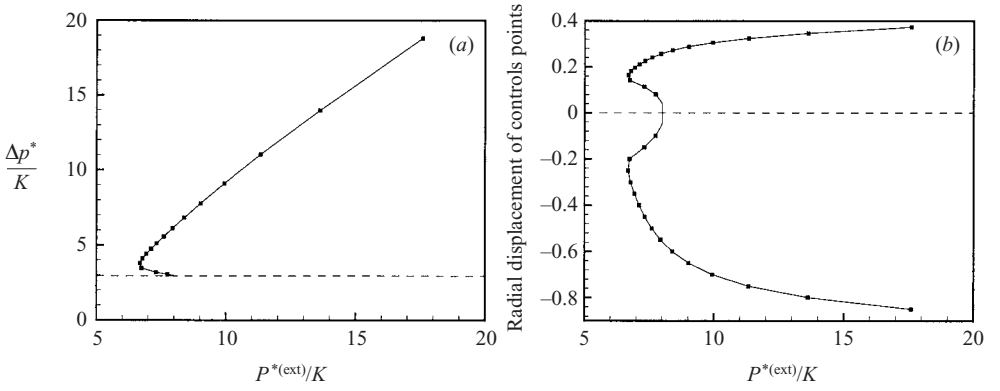

FIGURE 14. (*a*) Pressure drop along the entire system vs. external pressure for $Re_D = 350$ and $H = 10^4$. The results for a refined mesh are shown as symbols overlaid on the line. The dashed line is the pressure drop through the axisymmetric system. (*b*) Radial displacement of the control points in the symmetry planes at $\zeta^1 = 7.5$, vs. external pressure for the same system. The dashed line is the axisymmetric branch.

The computed velocity and pressure fields were compared with those postulated for a number of different values of the Reynolds number and mesh resolutions, using the global error norm

$$\mathscr{E} = \frac{1}{4}\left\{\sum_{i=1}^{3}\sqrt{\frac{\sum_n \left(u_{i_n} - u_{i_n}^{\dagger}\right)^2}{\sum_n \left(u_{i_n}^{\dagger}\right)^2}} + \sqrt{\frac{\sum_m (p_m - p_m^{\dagger})^2}{\sum_m (p_m^{\dagger})^2}}\right\},$$

where $\sum_{n/m}$ denotes the pointwise sum over the velocity/pressure nodes. Table 1 shows the values of $\mathscr{E}$ for three different mesh resolutions at $Re = 350$, illustrating the decrease of $\mathscr{E}$ with increasing resolution.

B.2. *Mesh refinement*

In order to validate the numerical results, we conducted the parameter study described in § 3.2.2 at a number of different mesh resolutions. H, Q and therefore Re_D were fixed and the external pressure $P^{(\mathrm{ext})}$, measured relative to the downstream fluid pressure, was used as the control parameter. In each study, the pressure was increased until the walls came close to opposite wall contact.

Figure 14(*a*) shows typical results for the pressure drop through the tube, $\Delta p = p_{\mathrm{up}} - p_{\mathrm{down}}$, as a function of the external pressure. At $P^{(\mathrm{ext})} = 0$, the tube is axisymmetric, actually slightly inflated, and the pressure drop follows from Poiseuille flow. As the external pressure increases, the tube remains axisymmetric until $P^{(\mathrm{ext})} \approx 8$, at which point it buckles non-axisymmetrically with a 'snap-through' bifurcation.

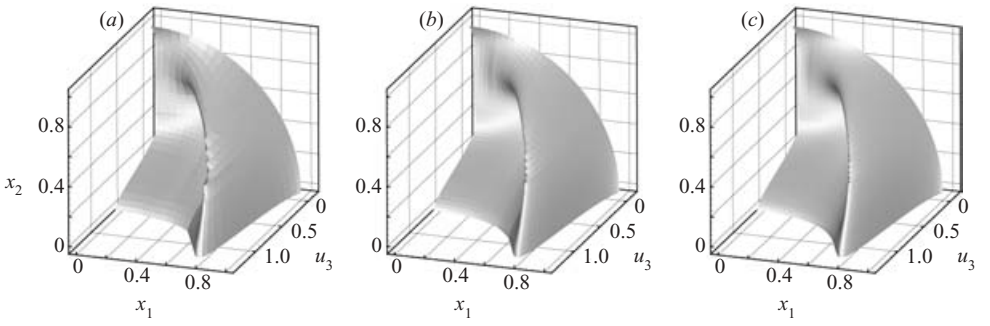

FIGURE 15. Axial velocity profiles at $x_3 = 10$ for $Re_D = 350$ and a strongly collapsed tube (*a*) 80 000 d.o.f.s, (*b*) 180 000 d.o.f.s, (*c*) 350 000 d.o.f.s. Note that although the jet is under-resolved at the coarsest resolution, the global flow features remain completely unchanged under mesh refinement.

The bifurcation may be seen more clearly in figure 14(*b*) which shows the radial displacement of two material points, $(\zeta^1, \zeta^2) = (7.5, 0)$ and $(7.5, \pi/2)$, on the tube surface plotted against $P^{(\mathrm{ext})}$. On losing stability, the tube immediately jumps into a strongly collapsed equilibrium configuration in which the minimum cross-sectional area is reduced by approximately 40% with an approximate doubling of the pressure drop. Further increasing the external pressure causes the tube to buckle more strongly and the pressure drop continues to increase, almost linearly with external pressure.

The lines in figure 14 were generated by using our standard resolution of ~80 000 degrees of freedom. The symbols were generated by using a finer mesh of ~180 000 degrees of freedom and the maximum relative error between the two sets of results is less than 0.05%.

The standard resolution is, therefore, perfectly adequate for the macroscopic parameter studies. On close inspection of the velocity fields, however, it was found that the standard resolution under-resolves (slightly) the boundary layers that develop in the strongly collapsed cross-sections at high Reynolds numbers. We therefore, used an even finer mesh of ~350 000 degrees of freedom to confirm the mesh independence of the flow features. The velocity profiles in the cross-section $x_3 = 10$, where the flow is at its most complex, are shown at all three resolutions in figure 15 and are practically indistinguishable.

REFERENCES

BATHE, K.-J. 1996 *Finite Element Procedures*, 2nd Edn. Prentice-Hall.

BENMBAREK, M. 1997 Ecoulement laminaire permanent dans un modele de veine. PhD thesis, L'Universite Paris XII.

BERTRAM, C. 1986 Unstable equilibrium behavior in collapsible tubes. *J. Biomech.* **19**, 61–69.

BERTRAM, C. D. 2002 Experimental studies of collapsible tubes. In *Flow in Collapsible Tubes and Past Other Highly Compliant Boundaries* (ed. P. W. Carpenter & T. Pedley), chap. 3, pp. 51–65. Kluwer.

BERTRAM, C. D. & CASTLES, R. J. 1999 Flow limitation in uniform thick-walled collapsible tubes. *J. Fluids Struct.* **13**, 399–418.

BERTRAM, C. D. & GODBOLE, S. A. 1997 LDA measurements of velocities in a simulated collapsed tube. *Trans. ASME: J. Biomech. Engng* **119**, 357–363.

BERTRAM, C. D., MULLER, M., RAMUS, F. & NUGENT, A. H. 2001 Measurements of steady turbulent flow through a rigid simulated collapsed tube. *Med. Biol. Engng Comput.* **39**, 422–427.

BOGNER, F. K., FOX, R. L. & SCHMIT, L. A. 1967 A cylindrical shell discrete element. *AIAA J.* **5**, 745–750.

Bonis, M. & Ribreau, C. 1978 Etude de quelques propriétés de l'écoulement dans une conduite collabable. *La Houille Blanche* **3**, 165–173.

Brower, R. W. & Scholten, C. 1975 Experimental evidence on the mechanism for the instability of flow in collapsible vessels. *Med. Biol. Engng* **13**, 839–845.

Cancelli, C. & Pedley, T. J. 1985 A separated-flow model for collapsible-tube oscillations. *J. Fluid Mech.* **157**, 375–404.

Conrad, W. A. 1969 Pressure–flow relationships in collapsible tubes. *IEEE Trans. Bio-med. Engng* **BME-16**, 284–295.

Duff, I. S. & Scott, J. A. 1996 The design of a new frontal code for solving sparse, unsymmetric linear systems. *ACM Trans. Math. Software* **22**, 30–45.

Ethier, C. R., Prakash, S., Steinman, D. A., Leask, R. L., Couch, G. G. & Ojha, M. 1999 Steady flow separation patterns in a 45 degree junction. *J. Fluid Mech.* **411**, 1–38.

Flaherty, J. E., Keller, J. B. & Rubinow, S. I. 1972 Post buckling behavior of elastic tubes and rings with opposite sides in contact. *SIAM J. Appl. Maths* **23**, 446–455.

Heil, M. 1996 The stability of cylindrical shells converying viscous flow. *J. Fluids Struct.* **10**, 173–196.

Heil, M. 1997 Stokes flow in collapsible tubes: computation and experiment. *J. Fluid Mech.* **353**, 285–312.

Heil, M. 1998 Stokes flow in an elastic tube – a large-displacement fluid-structure interaction problem. *Intl. J. Numer. Meth. Fluids* **28**, 243–265.

Heil, M. & Jensen, O. E. 2002 Flow in deformable tubes and channels: Theoretical models and biological applications. In *Flow in Collapsible Tubes and Past Other Highly Compliant Boundaries* (ed. P. W. Carpenter & T. Pedley), chap. 2, pp. 15–49. Kluwer.

Heil, M. & Pedley, T. J. 1996 Large post-buckling deformations of cylindrical shells conveying viscous flow. *J. Fluids Struct.* **10**, 565–599.

Jensen, O. E. & Pedley, T. J. 1989 The existence of steady flow in a collapsed tube. *J. Fluid Mech.* **206**, 339–374.

Kistler, S. F. & Scriven, L. E. 1983 Coating flows. In *Computational Analysis of Polymer Processing* (ed. J. R. A. Pearson & S. M. Richardson), pp. 243–299. Applied Science Publishers.

Kounanis, K. & Mathioulakis, D. S. 1999 Experimental flow study within a self oscillating collapsible tube. *J. Fluids Struct.* **13**, 61–73.

Lighthill, M. J. 1963 Attachment and separation in three-dimensional flows. In *Laminar Boundary Layers* (ed. L. Rosenhead), chap. II, § 2.6–2.7, pp. 72–82. Oxford University Press.

Luo, X. Y. & Pedley, T. J. 1995 Numerical simulation of steady flow in a 2-d collapsible channel. *J. Fluids Struct.* **9**, 149–197.

Luo, X. Y. & Pedley, T. J. 1996 A numerical simulation of unsteady flow in a two-dimensional collapsible channel. *J. Fluid Mech.* **314**, 191–225.

Luo, X. Y. & Pedley, T. J. 1998 The effects of wall inertia on flow in a two-dimensional collapsible channel. *J. Fluid Mech.* **363**, 253–280.

Luo, X. Y. & Pedley, T. J. 2000 Multiple solutions and flow limitation in collapsible channel flows. *J. Fluid Mech.* **420**, 301–324.

Naili, S., Thiriet, M. & Ribreau, C. 2002 Tridimensional flow in uniformly collapsed tubes: wall shear stress. *Eur. Phys. J. – Appl. Phys.* **17**, 139–153.

Ohba, K., Sakurai, A. & Oka, J. 1997 Laser doppler measurement of local flow field in collapsible tube during self-excited oscillation. *JSME Intl. J.* C **40**, 665–670.

Rast, M. P. 1994 Simultaneous solution of the navier–stokes and elastic membrane equations by a finite element method. *Intl. J. Numer. Meth. Fluids* **19**, 1115–1135.

Shapiro, A. H. 1977 Steady flow in collapsible tubes. *Trans. ASME: J. Biomech. Engng* **99**, 126–147.

Sobey, I. J. & Drazin, P. G. 1986 Bifurcations of two-dimensional channel flows. *J. Fluid Mech.* **171**, 263–287.

Taylor, C. & Hood, P. 1973 A numerical solution of the Navier-Stokes equations using the finite element technique. *Computers Fluids* **1**, 73–100.

Tobak, M. & Peake, D. J. 1982 Topology of three-dimensional separated flows. *Annu. Rev. Fluid Mech.* **14**, 61–85.

Wempner, G. A. 1973 *Mechanics of Solids*. McGraw–Hill.

Yamaki, N. 1984 *Elastic Stability of Circular Cylindrical Shells*. North-Holland.